

Comparison of Fully Coupled Immersed Boundary and Domain schemes for Fluid Structure Interaction with Lagrange Multipliers

Gabriele Marchi^[0009-0005-6930-2706] and

Rolf Krause^[0000-0001-5408-5271] and

Patrick Zulian^[0000-0002-5822-3288]

Abstract In this work, we consider fully coupled partitioned schemes for fluid–structure interaction (FSI) where the interaction between fluid and structure is enforced using distributed Lagrange multipliers. Within this framework, we compare two immersed approaches that differ in the choice of interaction domain: Immersed Boundary (IB) and Immersed Domain (ID) methods, illustrating the two formulations and numerically studying their differences in the context of FSI with thick structures. We analyze deviations between IB and ID solutions across a series of two-dimensional benchmark problems, investigating whether, and under which assumptions, the two formulations converge to the same solution as spatial and temporal resolutions are refined. In addition, we examine the number of sub-iterations required for convergence and identify the limitations of each approach under increasingly challenging flow regimes and boundary conditions. Overall, our study provides a simple and flexible framework for 2D FSI simulations, with publicly available code.

1 Introduction

Fluid-structure interaction (FSI) phenomena arise in numerous engineering and biological applications where the mutual coupling between a fluid flow and a deformable structure plays a crucial role. Examples range from cardiovascular biomechanics and aeroelasticity to offshore engineering and microfluidics. The computational modeling

Gabriele Marchi

Università della Svizzera italiana, Lugano, 6900, Ticino, Switzerland, e-mail: gabriele.marchi@usi.ch

Rolf Krause

King Abdullah University Of Science And Technology, Thuwal, 23955, Saudi Arabia, e-mail: rolf.krause@kaust.edu.sa

Patrick Zulian

Università della Svizzera italiana, Lugano, 6900, Ticino, Switzerland.
UniDistance Suisse, Brig, 3900, Switzerland e-mail: patrick.zulian@usi.ch

of FSI problems requires the numerical solution of coupled partial differential equations governing the fluid dynamics and structural mechanics, together with appropriate interface conditions. Two fundamentally different approaches exist for the numerical treatment of FSI problems: *boundary-fitted* (or body-conforming) and *non-fitted* (or immersed) methods. In boundary-fitted formulations, the computational mesh conforms to the fluid–structure interface throughout the simulation, typically relying on mesh motion strategies such as Arbitrary Lagrangian–Eulerian (ALE) techniques [6]. While these methods enable an accurate geometric representation of the interface and a natural enforcement of coupling conditions, their applicability is limited in the presence of large structural deformations or topological changes, where severe mesh distortion and frequent remeshing can significantly increase computational cost and algorithmic complexity. In contrast, non-fitted methods employ completely independent discretizations for the fluid and solid domains, with non-coinciding meshes and potentially different spatial and temporal discretization schemes [8, 10]. The solid moves through a fixed background fluid mesh, eliminating the need for mesh deformation and providing remarkable flexibility for problems with large deformations, contact, or multiple interacting bodies [14]. However, these methods face the challenge of accurately enforcing coupling conditions on non-conforming meshes. Among immersed approaches, the *Immersed Boundary* (IB) method, introduced by Peskin [15], distributes forces from Lagrangian markers to an Eulerian fluid grid via discrete delta functions. Alternatively, the *Fictitious Domain* method with distributed Lagrange multipliers [4, 2, 1], enforces kinematic coupling through a variational constraint, providing a rigorous mathematical framework and naturally accommodating for independent discretizations for the fluid, solid, and multiplier fields. Other immersed approaches include *penalty-based methods* [9]; the *immersed interface method* [11], which incorporates jump conditions for improved accuracy; *cut-cell methods* [16]; *extended finite element* (XFEM) approaches [7], which capture interface discontinuities via local mesh enrichment; the *Shifted Boundary Method* [12], which preserves high-order accuracy using a surrogate boundary; and *Nitsche-based formulations* [5], which weakly enforce interface conditions while maintaining stability.

In this work, we present a comparative study of the Immersed Boundary and Immersed Domain formulations for FSI problems discretized with distributed Lagrange multipliers. Both methods are formulated within a fully coupled scheme and solved using a partitioned solver strategy. The objective is to investigate their equivalence in the limit of mesh and time-step refinement, and analyze their convergence properties across different flow regimes.

2 Problem Description

We consider a fluid–structure interaction (FSI) problem in which a deformable solid body is immersed into an incompressible fluid. The fluid dynamics is governed by the incompressible Navier–Stokes equations, while the solid mechanics is described by the equations of elastodynamics. In the non-fitted mesh framework, the fluid equations are

posed over the entire domain $\Omega_f \subset \mathbb{R}^d$ ($d = 2, 3$), including the subdomain $\Omega_s(t) \subset \Omega_f$ occupied by the solid.

The interaction between fluid and solid is enforced through a kinematic coupling condition, which requires the continuity of fluid and solid velocities in a prescribed interaction domain $\mathcal{I}(t)$:

$$\mathbf{v}_f = \mathbf{v}_s (= \dot{\boldsymbol{\eta}}_s) \quad \text{in } \mathcal{I}(t), \quad (1)$$

where \mathbf{v}_f and \mathbf{v}_s denote the fluid and solid velocities, respectively, $\boldsymbol{\eta}_s$ is the solid displacement, and $\mathcal{I}(t)$ represents the region where the kinematic constraint is imposed.

Two major families of non-fitted mesh methods can be distinguished based on the choice of $\mathcal{I}(t)$. In *immersed domain* (ID) methods, the kinematic condition is enforced in the entire solid region, i.e. $\mathcal{I}(t) = \Omega_s(t)$, while in *immersed boundary* (IB) methods, the condition is imposed only on the solid boundary, i.e. $\mathcal{I}(t) = \partial\Omega_s(t)$. Since the fluid equations are formally defined also in $\Omega_s(t)$, IB methods leave the fluid velocity inside the solid region unconstrained, which may interfere with the correct enforcement of the FSI conditions.

In this work, we adopt a flexible framework for the numerical solution of the coupled FSI problem, based on a *fully coupled* formulation and a *partitioned* solution strategy. A *partitioned* strategy treats the two subproblems separately, relying on dedicated solvers for each physics, enabling the reuse of existing single-physics codes and provides flexibility in the design of the coupling algorithm [8, 10]. A *fully coupled* formulation refers to an approach in which the fluid and solid subproblems are solved in a strongly coupled manner at each time step, by iterating between the two until the interface coupling conditions are satisfied. This combination provides a strongly coupled framework, although appropriate time-step restrictions are required to ensure stability [8].

3 Numerical Methods

To enforce the kinematic condition (1), we adopt a distributed Lagrange multiplier framework, which provides a mathematically rigorous and flexible approach for the numerical treatment of fluid–structure interaction problems, allowing the coupling constraint to be enforced exactly at the discrete level. The Lagrange multiplier $\lambda : \mathcal{I}(t) \rightarrow \mathbb{R}^d$ represents the interaction force density exchanged between the fluid and the solid and naturally accounts for the coupling forces without penalty parameter tuning or artificial stabilization.

This section presents a general variational formulation of the coupled FSI problem based on the distributed Lagrange multiplier approach. Discretization, time integration, and implementation details are deferred to Section 3.2.

We express the coupled FSI problem in the following weak form: we seek fluid velocity \mathbf{v}_f , fluid pressure p_f , solid displacement $\boldsymbol{\eta}_s$, and Lagrange multiplier λ such that, for all admissible test functions $\delta\mathbf{v}_f$, δp_f , $\delta\boldsymbol{\eta}_s$, and $\delta\lambda$ in the corresponding function spaces, the following equations are satisfied:

$$\left(\rho_f \left(\frac{\partial \mathbf{v}_f}{\partial t} + (\mathbf{v}_f \cdot \nabla) \mathbf{v}_f \right) - \nabla \cdot \boldsymbol{\sigma}^f(\mathbf{v}_f, p_f), \delta \mathbf{v}_f \right)_{\Omega_f} - (\lambda, \delta \mathbf{v}_f)_{\mathcal{I}(t)} = 0, \quad (2)$$

$$(\nabla \cdot \mathbf{v}_f, \delta p_f)_{\Omega_f} = 0, \quad (3)$$

$$\left((\rho_s - \rho_f) \frac{\partial^2 \boldsymbol{\eta}_s}{\partial t^2} - \nabla \cdot \boldsymbol{\sigma}^s(\boldsymbol{\eta}_s), \delta \boldsymbol{\eta}_s \right)_{\Omega_s(t)} + (\lambda, \delta \boldsymbol{\eta}_s)_{\mathcal{I}(t)} = 0, \quad (4)$$

$$(\mathbf{v}_s - \mathbf{v}_f, \delta \lambda)_{\mathcal{I}(t)} = 0, \quad (5)$$

where $(\cdot, \cdot)_\Omega$ denotes the L^2 inner product over a domain Ω and $\boldsymbol{\sigma}^f$, $\boldsymbol{\sigma}^s$ are the fluid and solid stress tensors, respectively. In (4), the use of the density difference $(\rho_s - \rho_f)$ accounts for buoyancy effects [10] and ensures that the solid equation represents only the net inertia not already captured by the surrounding fluid.

The weak formulation (2)–(5) differs from the uncoupled fluid and solid problems only through three coupling terms: the interaction force $(\lambda, \delta \mathbf{v}_f)_{\mathcal{I}(t)}$ in the fluid equation, the reaction force $(\lambda, \delta \boldsymbol{\eta}_s)_{\mathcal{I}(t)}$ in the solid equation, and the kinematic constraint (5). This minimal modification preserves the structure of the individual subproblems and naturally lends itself to partitioned solution strategies.

After spatial and temporal discretization, the coupled problem can be written in algebraic form (6). For notational convenience, we collect the discrete fluid velocity and pressure unknowns into a single vector \mathbf{v}_f and denote the discrete solid velocity and Lagrange multiplier by \mathbf{v}_s and λ , respectively. The resulting system reads:

$$\begin{bmatrix} A_f & 0 & -B^\top \\ 0 & A_s & D^\top \\ -B & D & 0 \end{bmatrix} \begin{bmatrix} \mathbf{v}_f \\ \mathbf{v}_s \\ \lambda \end{bmatrix} = \begin{bmatrix} \mathbf{f}_f \\ \mathbf{f}_s \\ \mathbf{0} \end{bmatrix} \implies \begin{cases} A_f \mathbf{v}_f - B^\top \lambda = \mathbf{f}_f, \\ A_s \mathbf{v}_s + D^\top \lambda = \mathbf{f}_s, \\ -B \mathbf{v}_f + D \mathbf{v}_s = \mathbf{0}. \end{cases} \quad (6)$$

Here, A_f and A_s denote the discrete fluid and solid operators, including mass, convection, and diffusion or elasticity contributions, while \mathbf{f}_f and \mathbf{f}_s collect the contributions from external forces, boundary conditions, and previous time steps. Let $\{\phi_i^s\}_{i=1}^{N_s}$, $\{\phi_j^f\}_{j=1}^{N_f}$, and $\{\phi_k^\lambda\}_{k=1}^{N_\lambda}$ denote the basis functions for the solid, fluid, and Lagrange multipliers, respectively (see Section 3.2), the coupling matrices

$$B_{ij} := \int_{\mathcal{I}(t)} \phi_i^\lambda \cdot \phi_j^f \, d\gamma, \quad D_{ik} := \int_{\mathcal{I}(t)} \phi_i^\lambda \cdot \phi_k^s \, d\gamma. \quad (7)$$

enforce the kinematic constraint over the interaction domain $\mathcal{I}(t)$, mapping fluid and solid degrees of freedom to the Lagrange multiplier space, respectively.

3.1 Partitioned Solution Algorithm

The coupled system (6) can be solved either using a *monolithic* approach, which treats the two subproblems simultaneously, or a *partitioned* approach, which solves each subproblem independently with iterative coupling. Monolithic methods generally provide

superior robustness but require specialized saddle-point solvers and offer less flexibility for overconstrained situations, such as fluid–structure–contact interactions.

In this work, we adopt a partitioned strategy that decouples the fluid and solid subproblems while enforcing the coupling constraint exactly. At each time step, the interaction domain $\mathcal{I}(t)$ and the associated coupling operators B and D are computed from the previous solid configuration and then held fixed during sub-iterations until convergence. This avoids repeated reassembly of the operators, while ensuring accurate solutions for sufficiently small time steps. A representative partitioned solution procedure for (6) is summarized in Algorithm 1.

Algorithm 1 Partitioned iterative scheme with Lagrange multiplier-based coupling

```

1: for each time step  $n = 0, 1, 2, \dots$  do
2:   Compute interaction domain  $\mathcal{I}(t^n)$  from solid position  $\eta^s(t^n)$ 
3:   Assemble coupling operators  $B$  and  $D$  on  $\mathcal{I}(t^n)$ 
4:   while  $\|\lambda^{(k+1)} - \lambda^{(k)}\| > \varepsilon_{\text{tol}}$  do
5:     Compute solid velocity:  $\tilde{\mathbf{v}}_s = D^{-1}B\mathbf{v}_f^{(k)}$ 
6:     IB: Compute solid velocity satisfying Dirichlet BC  $\mathbf{v}_s^{(k+1)} = \tilde{\mathbf{v}}_s$  on  $\partial\Omega_s(t^n)$ 
7:     ID: Assume  $\mathbf{v}_s^{(k+1)} = \tilde{\mathbf{v}}_s$  on entire  $\Omega_s(t^n)$ 
8:     Update solid displacement and acceleration
9:     Compute Lagrange multiplier:  $\lambda^{(k+1)} = D^{-\top}(\mathbf{f}_s - A_s\mathbf{v}_s^{(k+1)})$ 
10:    Compute fluid velocity: Solve  $A_f\mathbf{v}_f^{(k+1)} = \mathbf{f}_f + B^\top\lambda^{(k+1)}$ 
11:   end while
12:   Set  $\mathbf{v}_f^{n+1} = \mathbf{v}_f^{(k)}$ ,  $\mathbf{v}_s^{n+1} = \mathbf{v}_s^{(k)}$ ,  $\lambda^{n+1} = \lambda^{(k)}$ 
13: end for

```

Steps 6–7 differ between the ID and IB methods: in the ID case, the transferred solid velocity $\tilde{\mathbf{v}}_s = D^{-1}B\mathbf{v}_f^{(k)}$ is enforced throughout the entire solid domain, whereas in the IB case, the velocity is imposed as a Dirichlet condition on $\partial\Omega_s(t^n)$ and the solid equation is solved to obtain the interior velocity field consistent with this boundary constraint. The convergence criterion is based on the change in Lagrange multiplier between successive sub-iterations, which provides a measure of the satisfaction of the kinematic constraint.

3.2 Spatial and Temporal Discretisation

For the fluid, we adopt a lowest-order finite volume (FV) scheme on a staggered Marker-and-Cell (MAC) grid. The resulting fluid velocities are cellwise constant, so the corresponding basis functions are simply indicator functions over each cell F_j . Time integration is performed using a partitioned explicit scheme based on Chorin’s projection method, which ensures incompressibility at each time step.

For the solid and the Lagrange multipliers, we employ bilinear finite elements on a structured mesh. The Lagrange multipliers are discretized on the same nodes as the solid: defined only on the boundary in the IB case, and over the full solid mesh in the ID

case. Time integration of the solid equations is performed using the Newmark- β scheme. In the IB approach, the elastodynamics equations are solved implicitly at each iteration, whereas the ID approach does not require a direct solution of the elastodynamics system. Instead, the solid response is computed through explicit updates of all kinematic and dynamic quantities at each time step within the Picard iteration.

3.3 Transfer Operator Implementation

In practice, we do not compute the Lagrange multiplier λ explicitly; instead, we directly evaluate $D^\top \lambda$ and transfer it to the fluid through the operator $B^\top D^{-\top} = (D^{-1}B)^\top$. This motivates the introduction of a single *transfer operator*

$$\mathcal{T} := D^{-1}B, \quad (8)$$

which maps fluid quantities onto the solid interface, while its transpose \mathcal{T}^\top transfers interface forces from the solid to the fluid.

To construct \mathcal{T} efficiently, we employ an L^2 quasi-projection [13] approximation of the weak equality conditions and we describe D by its diagonally lumped counterpart D^{lump} . According to the discretisation choices outlined above, the matrix D results to be the solid mass matrix restricted to the interaction domain $\mathcal{I}(t)$, while the matrix B simplifies to $B_{ij} = \int_{F_j} \phi_i^\lambda \, d\gamma$. Therefore the transfer operator (8) is given by

$$\mathcal{T}_{ij} \approx \frac{\int_{F_j} \phi_i^\lambda \, d\gamma}{D_{ii}^{\text{lump}}}. \quad (9)$$

This construction yields a local, conservative, and stable transfer operator without the use of regularized Dirac delta functions as in classical IB methods. The operator \mathcal{T} is assembled once per time step based on the current solid configuration and reused during nonlinear sub-iterations. The distinction between ID and IB approaches is reflected solely in the choice of $\mathcal{I}(t)$, leading to integrals over the solid domain (ID) or its boundary (IB), corresponding to area/line in 2D and volume/surface in 3D.

4 Numerical Experiments

We compare the Immersed Domain (ID) and Immersed Boundary (IB) methods within the framework described by Algorithm 1, adopting discretizations and transfer operator from Sections 3.2, 3.3. We assess the deviation between the solutions produced by the two approaches and investigate whether the two coupling formulations qualitatively converge to the same solution as the spatial and temporal resolutions are refined. We

also analyze the convergence behavior of the partitioned algorithm in terms of the number of sub-iterations required to enforce the kinematic coupling condition.

Unless otherwise stated, the same spatial resolution is employed for both the fluid and solid discretisations, and a convergence tolerance of 10^{-7} is used for the FSI iteration. For simplicity and clarity of presentation, all numerical experiments are conducted in two spatial dimensions and consider linear elastic solids, although the proposed framework can be extended to three-dimensional problems and hyperelastic models [3].

4.1 Floating Stiff Body in a Viscous Flow - $\text{Re} \sim 70$

We consider a stiff elastic body ($E = 10^6$, $\nu = 0.4$) freely floating in a viscous laminar flow. The thick solid, of size 0.5×0.5 , is immersed in a two-dimensional rectangular channel of size $[0, 5] \times [0, 1]$ with prescribed inflow and outflow boundary conditions. No-slip conditions are imposed on the top and bottom walls. The solid body is initially at rest and subsequently set into motion by the imposed flow.

For this first set of experiments, equal solid and fluid densities are assumed (density ratio = 1), while the robustness of the coupling strategies with respect to the solid-to-fluid density ratio is investigated in Table 1. Under this assumption, we assess the convergence behavior of the two coupling strategies by fixing one discretization parameter and varying the other. Specifically, Figure 1(a) reports the results obtained by fixing the spatial resolution Δx ($= \Delta x_s = \Delta x_f$) and progressively decreasing the time step Δt , while Figure 1(b) shows the complementary experiment in which Δt is fixed and Δx is progressively refined. For the present setup, fixing one discretization parameter and varying the other does not lead to a significant reduction in the discrepancy between the two solutions.

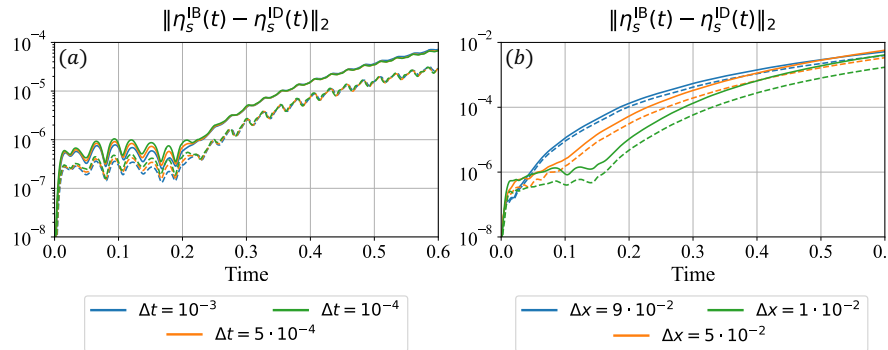


Fig. 1 Deviation of solid displacement fields between IB and ID formulations. Continuous lines indicate norm over the solid domain Ω_s , while dashed lines (--) refer to the solid boundary $\partial\Omega_s$. In panel (a), the time step Δt is varied while the spatial resolution is fixed at $\Delta x = 2 \cdot 10^{-2}$; in panel (b), the spatial resolution Δx is varied while the time step is fixed at $\Delta t = 5 \cdot 10^{-4}$. Parameters: $\rho_s = \rho_f = 1$, $\mu_f = 10^{-2}$, Young's modulus $E = 10^5$, and Poisson's ratio $\nu = 0.4$.

Motivated by the observed behavior, we next investigate the effect of simultaneous space–time refinement. To this end, we compare a coarse and a fine solution obtained by using, respectively, the coarsest and finest values of Δx and Δt considered in the previous refinement studies. As shown in Figure 2, the deviation on the solid boundary decreases by roughly one order of magnitude, while the overall change in resolution results in only a modest reduction in the solution difference.

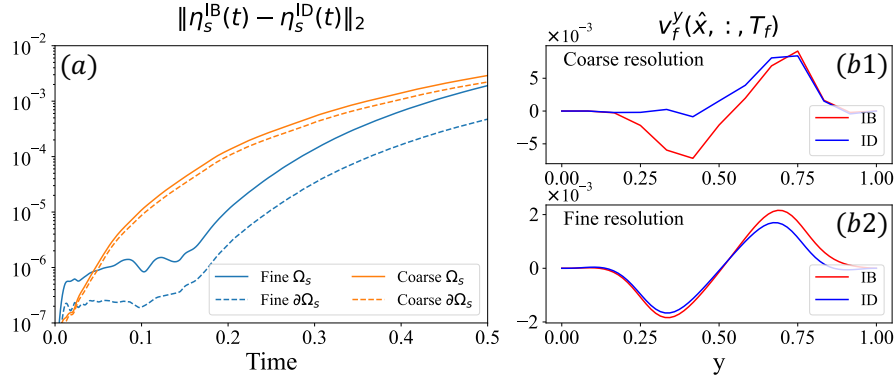


Fig. 2 Panel (a) shows the deviation between IB and ID solid displacement fields for two space–time resolutions: a coarse discretization with $(\Delta x, \Delta t) = (9 \cdot 10^{-2}, 10^{-3})$ and a fine discretization with $(\Delta x, \Delta t) = (10^{-2}, 10^{-4})$. Panels (b1) and (b2) present the y -component of the fluid velocity at the final time at a fixed \hat{x} location. This location lies downstream of the solid’s instantaneous position; the solid has already passed through it at an earlier time, and the observed velocity field corresponds to the flow disturbance induced by its prior motion. Panel (b1) corresponds to the coarse discretization, while panel (b2) corresponds to the fine discretization. Parameters: $\rho_s = \rho_f = 1$, $\mu_f = 10^{-2}$, Young’s modulus $E = 10^5$, and Poisson’s ratio $\nu = 0.4$.

Finally, Table 1 evaluates the robustness of the coupling strategies by reporting the error measures and the average number of sub-iterations required for convergence for different solid-to-fluid density ratios. For heavy solids, the ID formulation requires an increased number of sub-iterations to converge. In contrast, for density ratios close to or below unity, where *added-mass effects* [8] become significant, ID remains stable while IB exhibits convergence difficulties; common strategies to mitigate this issue include stabilization techniques such as relaxation or Aitken acceleration [8, 10].

Table 1 Average number of iterations per timestep and error between ID and IB for different solid-to-fluid density ratios. Parameters: $\Delta x = 2 \cdot 10^{-2}$, $\Delta t = 5 \cdot 10^{-4}$, $\mu_f = 10^{-2}$, $\rho_f = 10^{-1}$, $E = 10^5$, and $\nu = 0.4$. For density ratios below unity, the IB formulation fails to converge, corresponding error measures are therefore omitted.

ρ_s/ρ_f	10^3	10^2	10	1	0.9	0.5	10^{-2}
ID iterations	54	8	7	6	6	6	6
IB iterations	16	9	7	7	—	—	—
$\ \eta_s^{\text{IB}}(t) - \eta_s^{\text{ID}}(t)\ _2$ on $\partial\Omega_s$	$8 \cdot 10^{-4}$	$9 \cdot 10^{-4}$	$9 \cdot 10^{-4}$	$9 \cdot 10^{-4}$	—	—	—

4.2 Anchored Elastic Obstacle in a Laminar Channel Flow- $Re \sim 120$

This benchmark considers an elastic solid anchored to the bottom wall of a laminar channel flow. Compared to previous experiments, the solid-to-fluid density ratio is increased from 1 to 10, introducing significant solid inertia and an elastic response to flow-induced deformation. A parabolic inflow profile is prescribed at the inlet, smoothly ramped during the first 20% of the simulation time and then held constant. Standard outflow conditions are applied at the outlet, while no-slip conditions are enforced on the top and bottom walls.

The immersed solid has dimensions 0.3×0.4 and is initially at rest. Its lower boundary is anchored to the channel bottom. In our formulation, this anchoring requires no additional constraints: the solid velocity is obtained from the fluid, so the no-slip condition at $y = 0$ naturally enforces zero velocity and displacement at the solid nodes on the bottom boundary. When the solid mesh is coarser than the fluid mesh, the variational transfer may induce small spurious velocities at the anchored boundary due to neighboring unconstrained fluid cells; these can be eliminated by explicitly applying homogeneous Dirichlet conditions to the anchored solid nodes. The coupled fluid–structure interaction dynamics are investigated through two numerical experiments. First, Figure 3 illustrates the flow–structure interaction by showing the velocity field in the vicinity of the solid at selected time instants, highlighting both the deformation of the structure and its influence on the surrounding flow. Second, Figure 4 reports the time evolution of the horizontal and vertical displacements of three reference points located on the upper boundary of the solid.

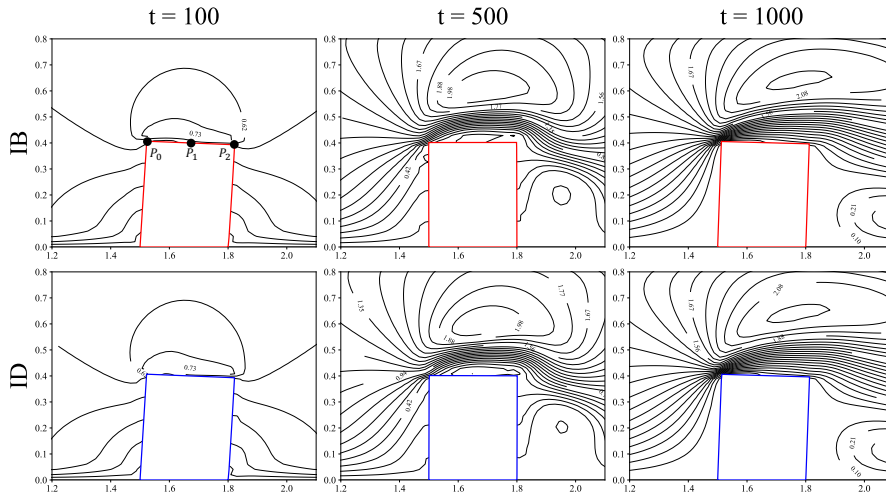


Fig. 3 Flow–structure interaction around the elastic solid at three selected time instants (columns). The first row shows the IB solution, the second row the ID solution. In each plot, the deformed solid is overlaid with the surrounding velocity field, illustrating the elastic deformation and its effect on the flow. Parameters: $\Delta x = 2 \cdot 10^{-2}$, $\Delta t = 10^{-3}$, $\rho_s = 10$, $\rho_f = 1$, $\mu_f = 0.01$, $E = 10^6$, $\nu = 0.4$.

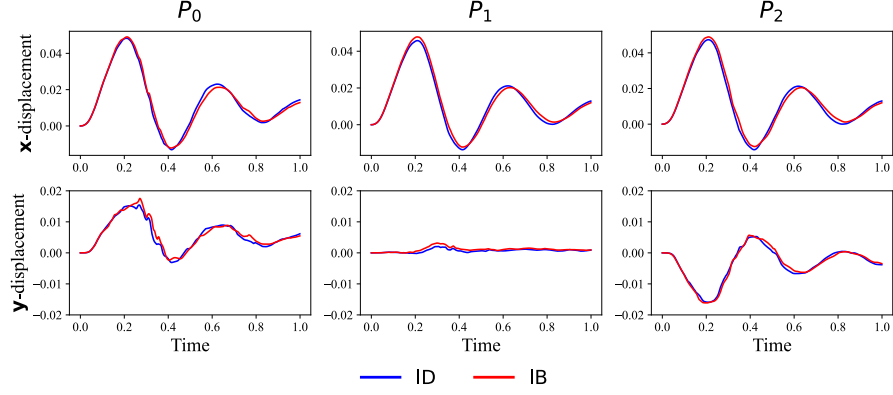


Fig. 4 Time evolution of the horizontal and vertical displacements of three reference points on the elastic solid: the top-left corner P_0 , a midpoint P_1 , and the top-right corner P_2 (Figure 3). Parameters: $\Delta x = 2 \cdot 10^{-2}$, $\Delta t = 10^{-3}$, $\rho_s = 10$, $\rho_f = 1$, $\mu_f = 0.01$, $E = 10^6$, and $\nu = 0.4$.

4.3 Comparison of Fluid Response with Fixed Obstacle- Re ~ 500

We consider a two-dimensional channel with a fixed obstacle positioned in the left portion of the domain. A prescribed inlet velocity generates the characteristic vortex shedding downstream of the obstacle. We compare the fluid response obtained using the Immersed Boundary (IB) and Immersed Domain (ID) methods with a reference solution, in which Dirichlet boundary conditions are strongly enforced along the obstacle surface.

In the FSI simulations, a zero-velocity constraint is applied to an internal region of the solid corresponding to approximately 20% of the obstacle area. In this way, the solid is anchored in its internal region, and by employing a high Young's modulus ($E = 10^6$), we effectively model a rigid obstacle.

Figure 5 shows the vorticity field at $T = 10$, illustrating the development of vortices behind the obstacle and highlighting the agreement between the IB, ID, and reference solutions. Overall, the IB method captures the vortex structures more accurately, while the ID approach tends to anticipate the vortex formation, resulting in vortices that are positioned farther downstream compared to the reference.

5 Conclusions

We presented a comparative study of Immersed Boundary (IB) and Immersed Domain (ID) formulations for FSI problems with thick structures using distributed Lagrange multipliers and an L^2 -quasi projection for the coupling operators.

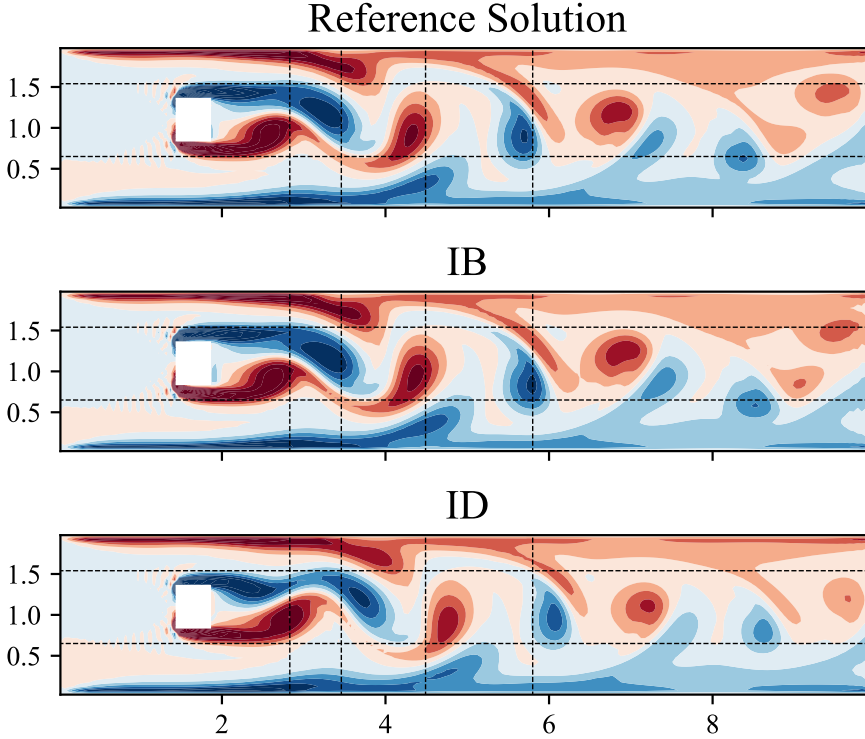


Fig. 5 Vorticity field at $T = 10$ and $\text{Re} \sim 500$ for the IB, ID, and reference solutions. Parameters: $\Delta x = 5 \cdot 10^{-2}$, $\Delta t = 10^{-3}$, $\rho_s = 10$, $\rho_f = 1$, $\mu_f = 0.004$, $E = 10^6$, and $\nu = 0.4$.

Our numerical experiments show that, at least for the cases considered, IB and ID exhibit similar overall behavior. The ID formulation appears more robust against low mass density ratios, while the IB approach is able to capture the fluid response more accurately.

Limitations of the present work include the use of only low-order discretizations, basic two-dimensional geometries, and moderate Reynolds numbers ($\text{Re} \lesssim 500$). Additionally, the study provides only a quantitative comparison between the two approaches, systematic validation against reference solutions is still missing in most test cases. Finally, the behavior of the solution inside the solid domain requires further investigation, particularly for the IB formulation, where the fluid velocity inside the solid remains unconstrained.

Future work will address these limitations through higher-order discretizations, more complex geometries, higher Reynolds number regimes, and extensions to three-dimensional problems with nonlinear constitutive models. Moreover, the development of ad hoc strategies to improve the stability and robustness of both methods will be pursued.

6 Acknowledgements & Software Availability

PZ and GM thank the SNSF project “Immersed Methods for Fluid–Structure–Contact Interaction Simulations and Complex Geometries” (nr.: 215627), and the PASC project “XSES-FSI: towards eXtreme scale Semi-Structured discretizations for Fluid–Structure–Interaction.” PZ thanks USI’s FIR. The developed software is publicly available at https://github.com/MarchGa/ENUMATH_Proceeding.

CRediT authorship contribution statement

GM: Conceptualization; Investigation; Methodology; Data Curation; Visualization; Software; Validation; Writing – Original Draft. PZ: Conceptualization; Methodology; Funding; Supervision; Writing – Review & Editing. RK: Writing – Review & Editing.

References

1. Alshehri, N., Boffi, D., Credali, F., Gastaldi, L.: Advances on finite element discretization of fluid–structure interaction problems. *Arab. J. Math.* (2025)
2. Baaijens, F.P.T.: A fictitious domain/mortar element method for fluid–structure interaction. *Int. J. Numer. Meth. Fluids* **35**, 743–761 (2001)
3. Boffi, D., Gastaldi, L., Heltai, L., Peskin, C.S.: On the hyper-elastic formulation of the immersed boundary method. *Comput. Methods Appl. Mech. Engrg.* **197**, 2210–2231 (2008)
4. Boffi, D., Gastaldi, L.: A fictitious domain approach with Lagrange multiplier for fluid–structure interactions. *Numer. Math.* **135**, 711–732 (2017). doi: 10.1007/s00211-016-0814-1
5. Burman, E., Fernández, M.A., Frei, S.: A Nitsche-based formulation for fluid–structure interactions with contact. *ESAIM: M2AN* **54**, 531–564 (2020)
6. Donea, J., Giuliani, S., Halleux, J.: An arbitrary Lagrangian–Eulerian finite element method for transient dynamic fluid–structure interactions. *Comp. Met. Appl. Mech. Eng.* **33**, 689–723 (1982)
7. Gerstenberger, A., Wall, W.A.: An eXtended finite element method/Lagrange multiplier based approach for fluid–structure interaction. *Comp. Met. Appl. Mech. Eng.* **197**, 1699–1714 (2008)
8. Hou, G., Wang, J., Layton, A.: Numerical methods for fluid–structure interaction – a review. *Mech. Aerospace Eng. Fac. Publ.* **64** (2012)
9. Huang, W.-X., Chang, C.B., Sung, H.J.: An improved penalty immersed boundary method for fluid–flexible body interaction. *J. Comput. Phys.* **230**, 5061–5097 (2011)
10. Kim, W., Choi, H.: Immersed boundary methods for fluid-structure interaction: A review. *Int. J. Heat Fluid Flow* **75**, 301–309 (2019)
11. LeVeque, R.J., Li, Z.: The immersed interface method for elliptic equations with discontinuous coefficients and singular sources. *SIAM J. Numer. Anal.* **31**, 1019–1044 (1994)
12. Main, A., Scovazzi, G.: The shifted boundary method for embedded domain computations. Part II: Linear advection–diffusion and incompressible Navier–Stokes equations. *J. Comput. Phys.* **372**, 996–1026 (2018)
13. Nestola, M.G.C., Becsek, B., Zolfaghari, H., Zulian, P., De Marinis, D., Krause, R., Obrist, D.: An immersed boundary method for fluid–structure interaction based on variational transfer. *J. Comput. Phys.* **398**, 108884 (2019)
14. Nestola, M.G.C., Zulian, P., Gaedke-Merzhäuser, L., Krause, R.: Fully coupled dynamic simulations of bioprosthetic aortic valves based on an embedded strategy for fluid–structure interaction with contact. *Europace* **23**, i96–i104 (2021).
15. Peskin, C.S.: The immersed boundary method. *Acta Numer.* **11**, 479–517 (2002)
16. Udaykumar, H.S., Shyy, W., Rao, M.M.: ELAFINT: A mixed Eulerian-Lagrangian method for fluid flows with complex and moving boundaries. *Int. J. Numer. Meth. Fluids* **22**, 691–712 (1996)